International Journal of Scientific Research & Engineering Trends
Volume 12, Issue 3, May-Jun-2026, ISSN (Online): 2395-566X

Experimental and Numerical Studies of Residual Stress Development on Alsi10mg Alloy Processed Through Powder Bed Fusion

Pankaj Kumar Rai[1], P. N. Ahirwar[2]
[1]Department of Mechanical Engineering Patel College of Science and Technology Bhopal, India.
[2]School of Mechanical Engineering Madhyanchal Professional University Bhopal, India

Abstract- Development of residual stresses during additive manufacturing (AM) imposes challenges on functionality and performance of the component. Being able to predict, measure and reduce residual stress by proper post processing will prevent pre-mature failure of the components. In this study finite element package of ANSYS software is employed to predict residual stress, distortion, melt pool dimensions and thermal history for the powder bed fusion (PBF) process of AM. Experimental validation of the residual stress predicted by the numerical modeling were carried out on additively manufactured coupon through X-ray diffraction. A small compressive residual stress on the top surface of the coupon is determined by both the experimental and numerical approach contradicting the reported work of tensile residual stress on the top surface.

Keywords- Additive Manufacturing, PBF, AlSi10Mg, Residual Stress, FEM.

I. INTRODUCTION

The Additive Manufacturing (AM) industry is growing at an exponential rate in today's time [1–3]. From customized product manufacturing for the biomedical sector to the mass production of aerospace components, AM is becoming an attractive choice for various industries [4,5]. The flexibility to generate intricate shapes, manufacturing of near net shape components and having comparable and in some cases even superior mechanical properties are some of the features that makes AM a prime choice over subtractive manufacturing [6–8].

Powder bed fusion (PBF) process produces high temperature and severe thermal gradient which results in distortion of the parts and accumulation of residual stress in the component [9–12]. The major concern of the industry is to predict and eliminate residual stress build up in the component during selective laser melting [13–16]. Tensile residual stresses are undesirable as they decrease the strength and fatigue resistance of the component by increasing the susceptibility of crack propagation [17,18]. Further the residual stress can induce more part distortion hampering the build accuracy [19].

Siddique et al. [20] had explained the effect of base plate preheating on residual stress while processing AlSi12 powder. It was found that residual stresses decrease when the base plate was heated to 200 oC to such an extent that stress relieving heat treatment did not have a remarkable impact. Wang et al. [21] had studied the effect of scanning strategy (chessboard and uniformity) and preheating the substrate on residual stress with AlSi10Mg component built by SLM. It was asserted that chessboard scanning strategy had much lower residual stress as compared to uniformity scanning strategy. Moreover, it was depicted that regardless of scanning strategy when the substrate preheating temperature was increased from 80 oC to 160 oC, there is a decrease in residual stress by 57%. Gusarov et al. [22] had used the thermo-elastic model in order to estimate the residual stress.

It was found that the maximum tensile stress in scanning direction was double of that in transverse direction. Rangaswamy et al. [23] had measured the residual stress by neutron diffraction and contour method revealing the presence of compressive stress at the centre and tensile stress at the sides. Vrancken et al. [24] had used X-ray diffraction technique for residual stress measurement in nine different material parts fabricated by SLM.

In the present work, macro-model analysis was carried out to determine the residual stress, melt pool dimension and thermal history characteristics. The residual stress that develops during the PBF process in the as-built components was evaluated through X-ray diffraction techniques. Further, numerical simulation of residual stress, distortion, melt pool characteristics and thermal history through finite element route.

II. EXPERIMENTAL DETAILS

Powder Bed Fusion process of additive manufacturing was employed to print the T-shape component using pre-alloyed AlSi10Mg powder on the AlSi10Mg base plate. The chemical composition of AlSi10Mg powder is given in Table 1. The geometry of the T shape specimen is present in Figure. 1 (a) which was modeled in SolidWorks. The CAD model was exported to the Materialize Magics Software for support geometry modeling. To create porous support, block, and cone type support (as shown in Figure. 1b) was used up to 3 mm in Z-direction of the base plate.

The support facilitates easy removal of specimen from the base plate and reduces specimen distortion while providing heat transfer routes during the build. The experiment was carried on EOSINT M280 having a build volume of 250*250*325 mm and is equipped with Ytterbium fibre laser. The process parameter for printing AlSi10Mg component is provided in Table 2. The inert environment inside the build chamber is maintained by continuous purging of argon gas. Figure. 2 depict the AlSi10Mg specimen attached to the AlSi10Mg substrate after fabrication in SLM machine.

Table 1. Chemical Composition of AlSi10Mg powder

Element	Al	Si	Fe	Cu	Mn	Mg	Ni	Zn	Pb	Sn	Ti
Weight%	Balance	9-11	0.55	0.05	0.45	0.2-0.45	0.05	0.1	0.05	0.05	0.15

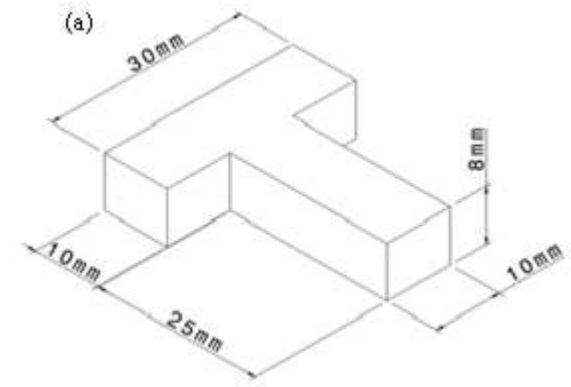

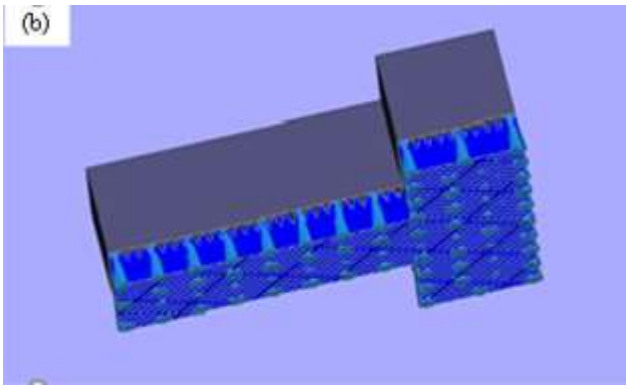

Figure. 1. (a) Geometry of the T shape speimen, and (b) Block & Cone support created in Materialise Software

Table 2. Process parameter for printing AlSi10Mg

Process Parameter	Values
Laser Power	370 W
Scan Speed	1300 mm/s
Layer Thickness	30 µm
Hatch Spacing	190 µm
Inter-Layer Rotation	67º
Pre-heat Temperature	165 ºC

The residual stress measurement was carried on X-ray diffractometer (PANalytical Empyrean diffractometer) with Cu-Kα (λCu = 1.54 Å) radiation was employed to measure the surface residual stress. Operating voltage and current for the stress scan were set at 45 kV and 40 mA respectively. The incident side of the diffractometer was having an X-ray lens and Ni filter, whereas the diffracted beam side was having parallel plate collimator with the detector in open mode. The sin2ψ method was adopted for stress analysis, conducting a total of 9 scans at a stage tilt angle (ψ) of 0, ± 18.43, ± 26.57, ±

33.21 and ± 39.23. The diffraction peak position for stress measurement was close to 137º of the crystallographic plane (422). The stage rotation angle (Φ), step size and dwell time for each scan were kept at 0º, 0.13º, and 10.56 s respectively. Stress software (PANalytical B.V., Netherlands) was used for the purpose of stress analysis.

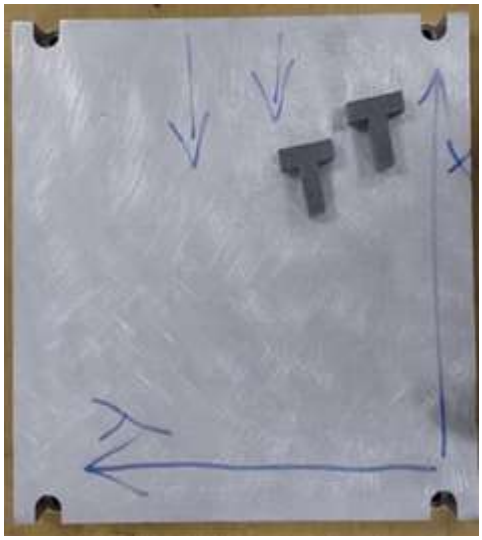

Figure. 2. Two T-shape AlSi10Mg specimen on AlSi10Mg substrate after the fabrication

Computational Modelling

3D numerical simulation of the selective laser melting based fabrication of the specimens was performed using the Additive Manufacturing suite of the ANSYS Workbench 2019 R1. For the additive manufacturing simulation in the ANSYS Workbench, a weak (Load type) thermomechanical coupling setup was formed. An independent non-linear transient thermal step calculates the temperature field which is followed by a static mechanical step using temperature solution in form of loads. The simulation was carried out using the same process parameters that was used to build the component experimentally. In order to demonstrate the process of layer-by-layer addition with time, element birth and death technique was used. First, the full built part modelled with 3D elements is kept in deactivated (death) state, and the elements are activated layer by layer.

To achieve element death effects, the elements are deactivated by multiplying its stiffness by severe reduction factor (1×10-6). The T-shape component was modelled using 8 nodded first order hexahedral elements. The finer mesh (Mean element size: 0.3mm) was selected for the built and the coarser mesh (Element size: 3 mm) was employed for the substrate. This resulted in 160888 elements for the built and 2187 elements for the base plate, and the number elements for support with element size of 0.3 mm was 61220 as shown in Figure. 3. The porous nature of support was incorporated in the modelling by using a multiplier of 0.4, that scale down its material property to 0.4 times of the original value. The connection between the base plate and the support is realized using a bonded contact.

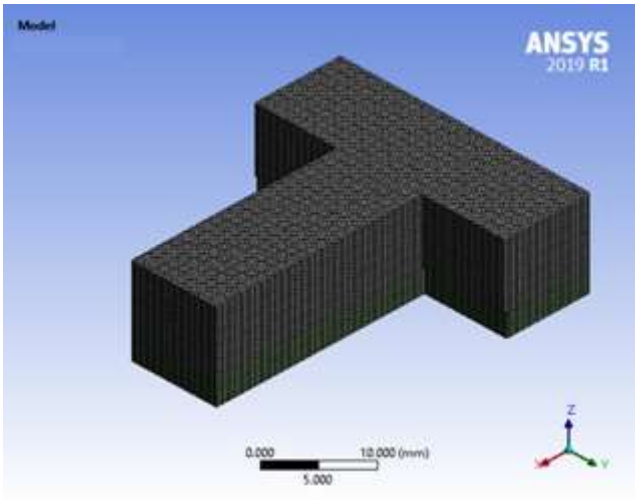

Figure. 3. Hexahedral mesh used for the built and support

Assumption

The following assumptions and conditions are taken in modelling the PBF process using ANSYS Additive Suite:

(1) Material is added and heated all at once for each element layer, i.e., scan pattern information was not used as input. The layer thickness in the experiment is very small (~30 µm), however, it is not practically possible to keep the element size this small. Hence, in simulation, layer thickness is larger and cannot be lesser than one element thickness.

(2) Instead of applying heat flux corresponding to the laser power, the new layer, characterized by the recently born elements, is initially set to the melt temperature of the AlSi10Mg material. This assumption is in line with the criteria of setting the process parameters (laser power and scan velocity) such that: (a) the developed temperature is always at or above melt (no lack of fusion) and (b) the developed temperature does not greatly exceed melt (no keyholing).

(3) Large integration time step was used throughout the simulation with a load step of 73 and substep of 20 for the transient thermal analysis and a load step of 74 and substep of

1 for the static structural analysis. This is sufficient to capture the induced thermal and plastic strains driving the distortion.

(4) The unmelted surrounding powder was not physically modelled, but in order to account for the heat loss, suitable convective boundary condition of at the interface between powder and solid material was used.

Thermal Analysis

The three-dimensional (3D) heat balance equation after substitution of Fourier conduction relation, is solved by the computational code used for heat transfer during additive manufacturing is given by,

$$\rho c \frac{\partial T}{\partial t} = \frac{\partial}{\partial x}\left(k \frac{\partial T}{\partial x}\right) + \frac{\partial}{\partial y}\left(k \frac{\partial T}{\partial y}\right) + \frac{\partial}{\partial z}\left(k \frac{\partial T}{\partial z}\right) + Q \quad (1)$$

where, ρ is the mass density (kg/m3), c is the specific heat capacity (J/kg.oC), T is the temperature (oC), t is time (s), k is the thermal conductivity (W/m.oC), and Q is the volumetric heat generation (W/m3). Q could be theoretically represented as moving heat source having a Gaussian profile.

$$Q = \frac{P}{\pi R_b^2 h} exp\left(1 - \frac{r^2}{R_b^2}\right)\left(1 - \frac{z}{h}\right)$$
$$r^2 = x^2 + y^2 + z^2 \quad (2)$$

where P is total power of the laser beam, Rb is the radius of the beam, h is the penetration depth and x, y, z are coordinates of the laser heat source at time t.

Prior to the melting of the powder bed at time t = 0, and long time after melting at t = ∞ the initial boundary condition was considered to have a uniform temperature distribution,

$$T(x, y, z, 0) = T_o = T(x, y, z, \infty) \quad (3)$$

To is the ambient temperature taken as 22 oC.

Both for the thermal and structural analysis, build step and cooldown step is considered. To account for the thermal boundary condition, heat loss to the un-melted powder and the gas in the chamber is approximated by considering a convective film coefficient of 10 W/m2.oC, both for the powder and gas. Apart from these, heat transfer from the base plate is consider by accounting the bottom face of the base plate. During the build phase, a temperature constraint equivalent to the preheat temperature of 165 oC is applied. After the printing process is complete, during the cooldown phase ambient temperature of 22 oC is applied at the bottom face of the base plate.

Mechanical analysis

The temperature solution in the form of loads is imported for the mechanical analysis. The boundary condition applied for the mechanical analysis is by fixing the motion of the bottom face. The stress distribution is calculated by using elastic finite element model given by:

$$\sigma = D\varepsilon^E \quad (4)$$

where σ is the stress tensor, D is the fourth order elastic tensor with temperature dependent Young's Modulus, E (N/m2) & Poisson ratio, ν and εE is elastic strain tensor. The elastic strain tensor is given by:

$$\varepsilon^E = \varepsilon - (\varepsilon^T + \varepsilon^P) \quad (5)$$

where ε is the total strain tensor, and εT & εP is the thermal strain and plastic strain respectively.

Therefore, the final stress and strain relationship can be given by:

$$\sigma = \sigma_{ex} + C\varepsilon^E \quad (6)$$

σex is the extra stress that accounts for the thermal and plastic stress. The thermal strain is given by:

$$\varepsilon^T = \alpha \Delta T = \alpha(T - T_0) \quad (7)$$

α is the temperature dependent coefficient of thermal expansion.

Temperature dependent material property

The temperature dependent thermos-physical properties and mechanical properties of AlSi10Mg considered for the simulation is provided in Table 3, Table 4, and Table 5. The solidus melting temperature for AlSi10Mg is set at 570 ºC.

Table 3. Temperature dependent mechanical properties of AlSi10Mg

Temperature (ºC)	Young's Modulus (MPa)	Temperature (ºC)	Coefficient of thermal expansion ($^oC^{-1}$)
25	76600	100	2.06e-5
50	76100	150	2.36e-5
100	74300	200	2.47e-5
150	72700	250	2.58e-5
200	70600	300	3.04e-5
250	68900	350	3.29e-5
300	67000	400	2.71e-5
		450	2.44e-5

Table 4. Thermo-physical properties of AlSi10Mg considered for the simulation

Temperature (°C)	Thermal Conductivity (W/m°C)	Temperature (°C)	Specific Heat (J/kg°C)	Temperature (°C)	Density (kg/m^3)
25	110	25	915	25	2670
50	111	150	1001	570	1710
100	112	275	1025		
150	114	425	1136		
200	113	550	1136		
250	109				
300	116				
400	116				
450	115				
500	109				
530	109				

Table 5. Bilinear Isotropic Hardening of AlSi10Mg considered for the simulation

Temperature (°C)	Yield Strength (MPa)	Tangent Modulus (MPa)
25	251	5000
100	232	4180
150	221	2430
200	197	1250
250	148	430

III. RESULTS AND DISCUSSION

Computational Result

The contour of the total deformation in the built specimen as obtained from the analysis is shown in Figure. 4 (a). The maximum deformation obtained is 0.31853 mm. Figure. 4 (b) provides the equivalent plastic strain distribution with the maximum value of 0.0040859. Figure. 4 (c) and (d) depicts the normal stress distribution profile in x and y direction respectively. The normal distribution in z direction is shown in Figure. 5 (a) The normal stress on the top surface of T-shape is provided in Figure. 5 (b). The normal (residual) stress on the top surface of the component is obtained to be compressive in nature at most of the locations with a value of -8.8926 MPa. Figure. 5 (c) provides the detail of the normal stress on one of the surfaces oriented perpendicular to the base. The top most layer is in tension with a stress of 20.4 MPa while, below this surface, material is under compression with a stress of -16.7 MPa. The equivalent (Von-Mises) stress distribution plot is provided in Figure. 5 (d).

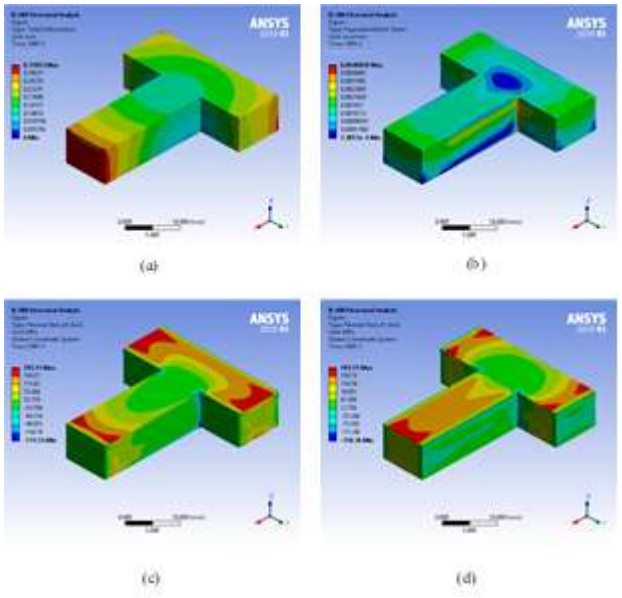

Figure. 4. Thermo-mechanical plots obtained from ANSYS Workbench simulation: (a) deformation plot, (b) elastic strain plot, (c) normal stress distribution along X-direction and (d) normal stress distribution along Y-axis.

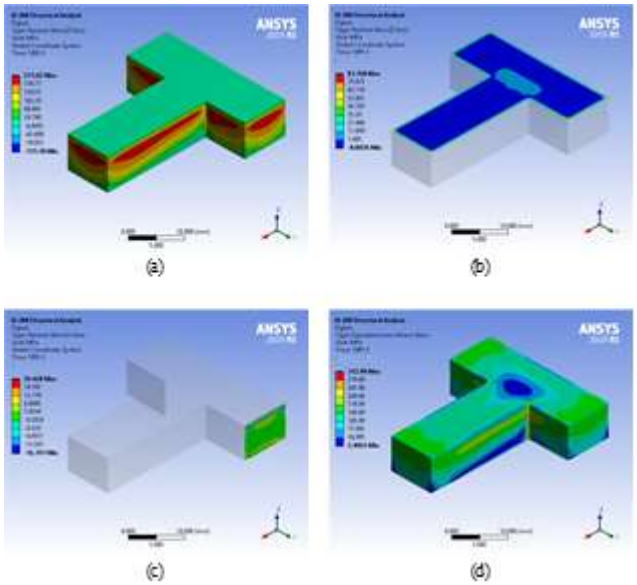

Figure. 5. Thermo-mechanical plots obtained from ANSYS Workbench simulation: (a) normal stress distribution along Z-direction, (b) normal stress distribution in XY plane, (c) normal stress distribution in XZ plane, and (d) Von-Mises stress distribution map.

Experimental Result

The experimental method provided the residual stress of -15.1±3.5 MPa in AlSi10Mg specimen. The residual stress measurement through X-ray diffraction revealed compressive stress on the top surface (surface parallel to the base plate) of the as-built component. This result was contradictory to results reported in literature depicting tensile stresses on the surfaces.

Melt Pool Characterization

A single bead parametric simulation was performed in ANSYS Additive Science Suite to obtain the information about melt pool characteristics of AlSi10Mg component. The effect of process parameters on the geometry of melt pool, i.e. melt pool length, melt pool width, and melt pool depth was determined. For determining melt pool characteristics input in the form of base plate preheating temperature of 165 ºC, layer thickness of 30 µm, laser power of 370 W and scan speed of 1300 mm/s was provided. The melt pool analysis was carried out on a bead length of 3 mm. Table 6 provides the information regarding the linear dimensions of the of the melt pool. Figure. 6 shows the plot of melt pool characteristics along the bead length. It is observed that melt pool dimension converges to steady state within 0.5 mm distance.

Table 6. Melt Pool Dimensions

Melt Pool Characteristics	Dimension (mm)
Melt Pool Length	0.367
Melt Pool Width	0.251
Melt Pool Depth	0.113

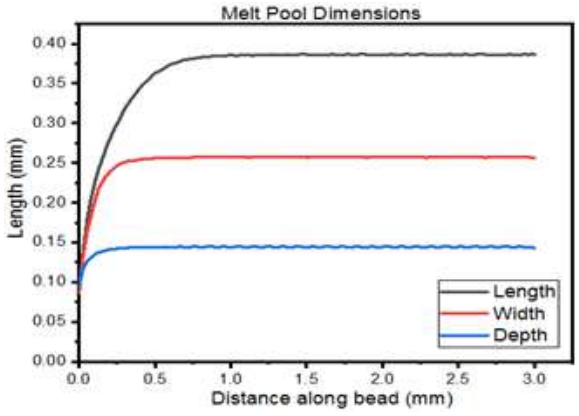

Figure. 6. Melt Pool Characteristics

In this thermal history simulation, information regarding the insights of the part in detail is provided. Different thermal conditions present in different regions of the part leads to hot and cold region that may be indicative of hot cracking, delamination, and porosity. The coaxial average sensor provides the map of the instantaneous melt pool dimensions (length, width and depth) and average temperature within a circular field of view centred about the laser position at the top surface of the part. The output includes a single 2D set of .vtk data for each deposit layer within the height range specified. These .vtk format data were imported to Paraview open-source software to obtain the thermal history plots. For performing the simulation, the geometry of the built is imported in .stl file. The simulation parameters are presented in Table 7. Figure. 7 (a), (b) and (c) provide the plot for melt pool dimensions with the maximum length of 0.49 µm, maximum depth of 0.15 µm and maximum width of 0.3 µm. Figure. 7 (d) shows the plot for temperature distribution with a maximum temperature of 350 ºC.

Table 7. Thermal History simulating parameters

Parameters	Value
Sensor Radius	0.5 mm
Sensor Z Height Range	0 mm – 10 mm
Baseplate temperature	175ºC
Laser Power	380 W
Scan Speed	1200 mm/s
Layer Thicknesss	30 µm
Starting Layer Angle	0º
Layer Rotation Angle	67º
Hatch Spacing	180 µm
Slicing Stripe Width	10 mm

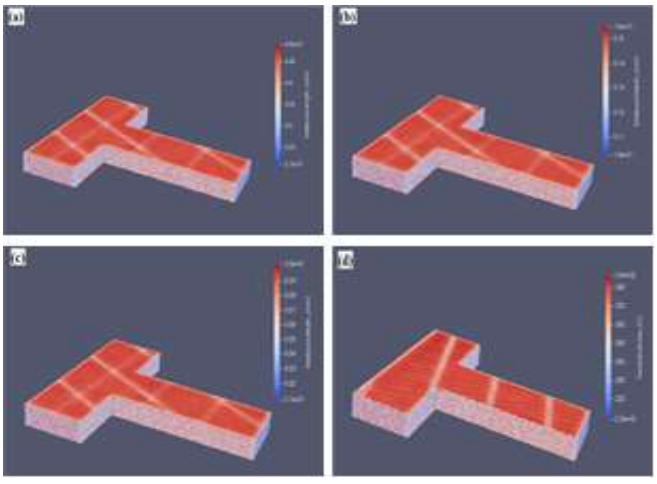

Figure. 7. Thermal history results showing melt pool characteristics (a) melt pool length, (b) melt pool depth, (c) melt pool width, and (d) temperature plot during the build.

Comparison between Simulation and Experimental results
The finite element analysis and the simulation predicted the residual stress in the AlSi10Mg part that was quite close to the experimental residual stress result. The residual stress measurement through X-ray diffraction revealed compressive stress of magnitude -15.1 MPa on the top surface (surface parallel to the base plate) of the as-built component. This result was contradictory to results reported in literature depicting tensile stresses on the surfaces. The simulation analysis in ANSYS predicted a result of -8.89 MPa on the top surface of the component. Figure. 8 depicts the comparison between experimental and simulation result.

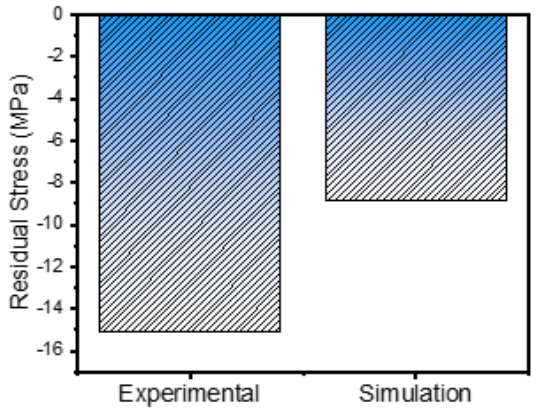

Figure. 8. Comparison between Experimental and Simulation result

V. CONCLUSION

In this work through finite element modeling and simulation in ANSYS software the distortion, residual stress, melt pool characteristics and thermal history were measured. The findings in this investigation are discussed below:

(1) The residual stress measurement through X-ray diffraction revealed compressive stress on the top surface (surface parallel to the base plate) of the as-built component. This result was contradictory to results reported in literature depicting tensile stresses on the surfaces.

(2) The finite element analysis and the simulation predicted the residual stress in the AlSi10Mg part that was quite close to the experimental residual stress result. The melt pool characteristics such as melt pool depth, width and length was quite accurately determined by the simulation. The thermal history results showed the temperature distribution and the maximum temperature that develops during the printing process.

Declarations
Funding
This study was not supported by any funding

Ethics approval and consent to participate
Not applicable.

Consent for publication
Not applicable.

Competing interests
The authors declare that they have no known competent financial interest or personal relationships that could have appear to influence the reported work.

Data availability statement
Data available on request.

REFERENCES

1. Dejene, N. D., and Lemu, H. G., 2024, “Characterisation and Prediction of Mechanical Properties in Laser Powder Bed Fusion-Printed Parts : A Comparative Analysis Using Machine Learning,” Mater. Technol., 39(1).
2. Su, J., Jiang, F., Teng, J., Chen, L., Requena, G., Yan, M., Zhang, L., Wang, Y. M., Okulov, I. V, Zhu, H., Bo, G., Chew, Y., and Tan, C., 2024, “Laser Additive Manufacturing of Titanium Alloys: Process, Materials and Post-Processing,” Rare Met., 43(12), pp. 6288–6328.
3. Pourrahimi, S., and Hof, L. A., 2024, “On the Post-Processing of Complex Additive Manufactured Metallic Parts A Review,” Adv. Eng. Mater., 26(2301511).
4. Singh, V. K., Sahoo, D., Ranjan, A., Amirthalingam, M., Karagadde, S., and Mishra, S. K., 2025, “Comparison of Tensile and LCF Behaviour of Heat-Treated Inconel 718 Printed by LPBF and LW-DED at Different Temperatures,” Int. J. Fatigue, 198(April), p. 109010.
5. Singh, V. K., Sahoo, D., Amirthalingam, M., Karagadde, S., and Mishra, S. K., 2024, “Dissolution of the Laves Phase and δ-Precipitate Formation Mechanism in Additively Manufactured Inconel 718 during Post Printing

Heat Treatments," Addit. Manuf., 81(February), p. 104021.

6. DebRoy, T., Wei, H. L., Zuback, J. S., Mukherjee, T., Elmer, J. W., Milewski, J. O., Beese, A. M., Wilson-Heid, A., De, A., and Zhang, W., 2018, "Additive Manufacturing of Metallic Components – Process, Structure and Properties," Prog. Mater. Sci., 92, pp. 112–224.
7. Kempen, K., Thijs, L., Van Humbeeck, J., and Kruth, J. P., 2012, "Mechanical Properties of AlSi10Mg Produced by Selective Laser Melting," Phys. Procedia, 39, pp. 439–446.
8. Zhang, L. C., Attar, H., Calin, M., and Eckert, J., 2016, "Review on Manufacture by Selective Laser Melting and Properties of Titanium Based Materials for Biomedical Applications," Mater. Technol., 31(2), pp. 66–76.
9. Arunprasath, K., Shanawaz, A. M., Kavitha, S., Narayanaperumal, S., Bobby, S. S., and Velmurugan, G., 2026, "Metallic Additive Manufacturing : State-of-the-Art , Process-Structure-Property Relationships , and Emerging Trends," J. Mater. Res. Technol., 42(March), pp. 1241–1275.
10. Ni, C., Zhu, J., Zhang, B., An, K., Wang, Y., Liu, D., Lu, W., Zhu, L., and Liu, C., 2025, "Recent Advance in Laser Powder Bed Fusion of Ti – 6Al – 4V Alloys : Microstructure , Mechanical Properties and Machinability," Virtual Phys. Prototyp., 20(1), pp. 1–39.
11. Chen, H., Cheng, T., Li, Z., Wei, Q., and Yan, W., 2022, "Is High-Speed Powder Spreading Really Unfavourable for the Part Quality of Laser Powder b e d Fusion Additive Manufacturing ?," Acta Mater., 231, p. 117901.
12. Shahed, K., Meinert, K., Yilmaz, B., Lear, M., and Manogharan, G., 2025, "Multi-Material Laser Powder Bed Fusion : Effects of Build Orientation on Defects , Material Structure and Mechanical Properties," npj Adv. Manuf. Manuf., 2(5), pp. 1–11.
13. Shao, Z., Zhang, C., Li, Y., Shen, H., Zhang, D., Yu, X., and Zhang, Y., 2022, "A Review of Non-Destructive Evaluation (NDE) Techniques for Residual Stress Profiling of Metallic Components in Aircraft Engines," Aerospace, 9(10).
14. Zhan, Y., Liu, C., Zhang, J., Mo, G., and Liu, C., 019, "Measurement of Residual Stress in Laser Additive Manufacturing TC4 Titanium Alloy with the Laser Ultrasonic Technique," Mater. Sci. Eng. A, 762(July), p. 138093.
15. Mukherjee, T., Zhang, W., and DebRoy, T., 2017, "An Improved Prediction of Residual Stresses and Distortion in Additive Manufacturing," Comput. Mater. Sci., 126, pp. 360–372.
16. Wang, S., Li, Y., Yao, M., and Wang, R., 1998, "Compressive Residual Stress Introduced by Shot Peening," J. Mater. Process. Technol., 73(1–3), pp. 64–73.
17. Mercelis, P., and Kruth, J. P., 2006, "Residual Stresses in Selective Laser Sintering and Selective Laser Melting," Rapid Prototyp. J., 12(5), pp. 254–265.
18. Wagner, L., 1999, "Mechanical Surface Treatments on Titanium, Aluminum and Magnesium Alloys," Mater. Sci. Eng. A, 263(2), pp. 210–216.
19. Zäh, M. F., and Lutzmann, S., 2010, "Modelling and Simulation of Electron Beam Melting," Prod. Eng., 4(1), pp. 15–23.
20. Siddique, S., Imran, M., Wycisk, E., Emmelmann, C., and Walther, F., 2015, "Influence of Process-Induced Microstructure and Imperfections on Mechanical Properties of AlSi12 Processed by Selective Laser Melting," J. Mater. Process. Technol., 221, pp. 205–213.
21. Wang, L., Jiang, X., Zhu, Y., Ding, Z., Zhu, X., Sun, J., and Yan, B., 2018, "Investigation of Performance and Residual Stress Generation of AlSi10Mg Processed by Selective Laser Melting," Adv. Mater. Sci. Eng., 2018.
22. Gusarov, A. V., Pavlov, M., and Smurov, I., 2011, "Residual Stresses at Laser Surface Remelting and Additive Manufacturing," Phys. Procedia, 12(PART 1), pp. 248–254.
23. Rangaswamy, P., Griffith, M. L., Prime, M. B., Holden, T. M., Rogge, R. B., Edwards, J. M., and Sebring, R. J., 2005, "Residual Stresses in LENS® Components Using Neutron Diffraction and Contour Method," Mater. Sci. Eng. A, 399(1–2), pp. 72–83.
24. Vrancken, B., Wauthle, R., Kruth, J. P., and Van Humbeeck, J., 2013, "Study of the Influence of Material Properties on Residual Stress in Selective Laser Melting," 24th Int. SFF Symp. - An Addit. Manuf. Conf. SFF 2013, pp. 393–407.